

Title	Periodic Grain-Boundary Formation in a Poly-Si Thin Film Crystallized by Linearly Polarized Nd:YAG Pulse Laser with an Oblique Incident Angle
Author(s)	Kaki, H; Horita, S
Citation	Journal of Applied Physics, 97(1): 014904-1-014904-9
Issue Date	2005-01
Type	Journal Article
Text version	publisher
URL	<a href="http://hdl.handle.net/10119/3378">http://hdl.handle.net/10119/3378</a>
Rights	Copyright 2005 American Institute of Physics. This article may be downloaded for personal use only. Any other use requires prior permission of the author and the American Institute of Physics. The following article appeared in Hirokazu Kaki and Susumu Horita, Journal of Applied Physics 97(1), 014904 (2005) and may be found at <a href="http://link.aip.org/link/?jap/97/014904">http://link.aip.org/link/?jap/97/014904</a> .
Description	

# Periodic grain-boundary formation in a poly-Si thin film crystallized by linearly polarized Nd:YAG pulse laser with an oblique incident angle

Hirokazu Kaki<sup>a)</sup> and Susumu Horita

*Japan Advanced Institute of Science and Technology, 1-1 Asahidai, Tatsunokuchi, Ishikawa 923-1292, Japan*

(Received 20 July 2004; accepted 5 October 2004; published online 10 December 2004)

We investigated the periodic grain-boundary formation in the polycrystalline silicon film crystallized by a linearly polarized Nd:YAG (where YAG is yttrium aluminum garnet) pulse laser with an oblique incident angle  $\theta_i=25^\circ$ , compared with the normal incident angle  $\theta_i=0$ . The alignment of the grain boundary was uncontrollable and fluctuated in the case of the oblique incident and large irradiation pulse number while that in the case of the normal incident was performed stably. It was found that the main cause for its low controllability was the nonphase matching between the periodic surface corrugation of the crystallized silicon film and the periodic temperature profile induced by the laser irradiation. Also, it was found that, in the case of  $\theta_i=25^\circ$ , the dominant periodic width of the grain boundary depended on the pulse number  $N$ . That is, it was around  $\lambda/(1+\sin \theta_i)$  for small  $N \approx 10$  and  $\lambda/(1-\sin \theta_i)$  for large  $N \approx 100$  at the laser wavelength of  $\lambda=532$  nm. In order to explain this dependence, we proposed a model to take into account the periodic corrugation height proportional to the molten volume of the silicon film, the impediment in interference between the incident beam and diffracted beam on the irradiated surface due to the corrugation height, and the reduction of the liquid surface roughness during melting-crystallization process due to liquid-silicon viscosity. © 2005 American Institute of Physics.

[DOI: 10.1063/1.1827915]

## I. INTRODUCTION

Low-temperature polycrystalline silicon (poly-Si) thin-film transistors (TFTs) are widely used for various applications such as driver circuits of active matrix liquid-crystal displays and active matrix organic light-emitting diode displays. Moreover, system on panel displays in which the system circuits of the controller and memory are integrated with the driver circuits on a glass substrate will be the most suitable application for poly-Si TFTs in the near future. A pulse laser annealing (PLA) method is effective to produce a poly-Si film of larger grain with high carrier mobility on an inexpensive glass substrate.<sup>1,2</sup> However, ideal TFTs require active regions entirely free of grain boundary which reduces the carrier mobility, fluctuates the threshold voltage, and increases the off current of the transistors. In order to suppress the generation of the grain boundary, it is necessary to control the temperature profile in the Si film so as to reduce random nucleation and unify the solidification direction of the molten Si. Some researchers have proposed modulated PLA methods to use absorption layer,<sup>3,4</sup> prepatterned Si layer,<sup>5</sup> or so on.<sup>6-9</sup> The interference PLA methods to use a beam splitter<sup>10</sup> or a phase-shift mask<sup>11</sup> have also been developed. However, these methods require additional fabrication processes or optical components.

On the other hand, we have reported that, using spatially periodic temperature profile induced by linearly polarized laser beam irradiation, we can control the location of grain boundaries in the Si film crystallized on a Pyrex glass substrate. That is to say, the straight lines of the grain boundary

are aligned parallel to each other with a constant distance near the wavelength of the laser beam and are perpendicular to the electric field of the incident beam.<sup>12</sup> The periodicity  $\Lambda$  of the temperature profile or grain boundary is formulated from Rayleigh's diffraction conditions as

$$\Lambda \approx \lambda / [n_0(1 \pm \sin \theta_i)] \quad (1)$$

for a  $p$ -polarized beam, where  $\lambda$  is the incident laser wavelength,  $\theta_i$  is the incident angle from the normal incidence, and  $n_0$  is the refractive index of the incident medium above the surface.<sup>13-18</sup> This laser crystallization method has advantages over the conventional modulated PLA methods. It does not require any additional processes such as patterning of the substrate and forming of the absorption or antireflection layer, and additional optical components, which leads to reduction in the processing time and manufacturing cost.

Further, we have reported the influence of the irradiation conditions of the polarization of the laser beam, the incident angle, the pulse number, the energy density, and so on, on both melting crystallization and controllability of the periodic grain-boundary location in the crystallized Si film.<sup>19</sup> From this investigation, we concluded that the linear polarization of the laser beam and the periodic surface roughness of the irradiated sample were key factors in the formation of the periodic grain boundary. However, we found the next two strange phenomena. First,  $\Lambda$  of the grain boundary on the crystallized Si film was increased with  $\theta_i$  for the pulse number  $N > 10$  as the only  $\lambda/(1-\sin \theta_i)$  component of Eq. (1). Second, although the increase of the  $\Lambda$  is favorable for the fabrication of electron devices, the controllability of the grain-boundary location was lowered with increasing  $\theta_i$  and

<sup>a)</sup>Electronic mail: h-kaki@jaist.ac.jp

the line of the grain-boundary becomes not straight but curved. In order to find out the mechanism for the above phenomena, we researched the grain-boundary formation in the Si film melting crystallized with an oblique incident angle  $\theta_i=25^\circ$  in detail. In this paper, we show the experimental data and compare them with the two-dimensional finite element computer simulation to take into account heat transport and phase transitions during laser irradiation. Then, we propose a model to explain them rationally.

## II. THEORETICAL ANALYSIS

### A. Periodic laser energy density on the sample surface

At first, we analyze the periodic laser energy density on the irradiated surface of the Si film. The temperature profile which determines the direction of crystal growth is governed by this periodic laser energy density. The periodic laser energy density is generated by the periodic surface roughness of the Si film. An as-deposited Si film does not have a periodic but a random surface roughness with a very small height, as will be shown later. Since this random surface roughness is composed of surface gratings with many various spatial periods, it might have a spatial periodicity component to produce a diffracted beam traveling on the surface according to Eq. (1). The intensity of this traveling beam is modified by the surface roughness with the spatial periodicity component. This modification resulted from the interaction of waves between the primary incident beam and the diffracted beam so that it produces the periodic laser energy density. The surface roughness of the spatial component is slightly increased at the first pulse due to the small amplitude of the periodic laser energy density. The mechanism of the surface roughness increment is mentioned elsewhere.<sup>16,19</sup> An increased surface roughness leads to the increase of the diffracted beam intensity, which leads to the increase of the modulation of the incident-beam intensity and the amplitude of the periodic laser energy density. Thus, the modification of the surface roughness and laser energy density is enhanced with the positive feedback loop.

Our analysis is based on the theoretical report by Guosheng *et al.* on the laser energy density profile on the periodically corrugated surface of the sample.<sup>20</sup> This corrugated surface is the same as the surface roughness with the spatial

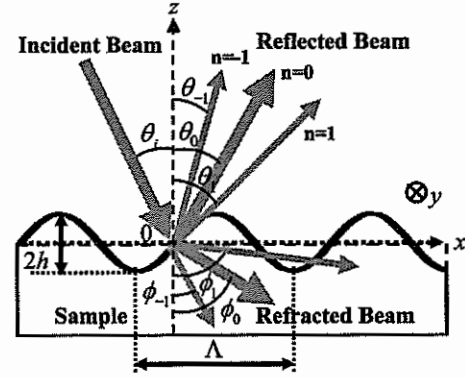


FIG. 1. Schematic drawing of the diffraction of an incident beam from a corrugated surface. A plane wave or linearly polarized laser beam is incident on the surface with an angle of incidence  $\theta_i$ . The reflected and the refracted waves are generated due to the diffraction of an incident wave. The angles of the  $n$ th-order reflected and refracted waves are  $\theta_n$  and  $\phi_n$ , respectively.

periodicity component as mentioned above. The diffraction of the incident laser beam occurs on a sinusoidally corrugated surface, as illustrated in Fig. 1. The corrugated vacuum-solid interface is described by the following surface equation:

$$z(x) = -h \cos \frac{2\pi}{\Lambda} x, \quad (2)$$

where  $h$  is the amplitude of the corrugation, the  $z$  axis is outward normal to the macroscopic surface, and the  $x$  axis is perpendicular to the corrugation. A plane wave or linearly polarized laser beam is incident on the surface with  $\theta_i$ . Then, the reflected and the refracted waves are generated due to diffraction of the incident wave. The angles of the  $n$ th-order reflected and refracted waves are  $\theta_n$  and  $\phi_n$ , respectively.

The Poynting vector modulated by the diffraction can be calculated from standard diffraction theory and the normal component of the average Poynting vector,  $P_n$ , just inside the medium can be expressed as

$$P_n = P_0 \left[ 1 + P_1 \cos \left( \frac{2\pi}{\Lambda} x - \phi_p \right) \right], \quad (3)$$

where  $P_0 > 0$  and  $P_1 > 0$  are a dc or average component and an ac amplitude ratio, respectively, and  $\phi_p$  is the phase difference between the sinusoidal surface corrugation and  $P_n$ . The ac term  $P_1$  comes from the interaction between waves of

TABLE I. Material parameters used in the simulations.  $\alpha$ ,  $n$ ,  $\kappa$ ,  $L$ ,  $T_m$ ,  $\rho$ ,  $c_p$ , and  $K$  denote the absorption coefficient, the refractive coefficient, the attenuation coefficient, the latent heat, the phase change temperature, the density, the specific heat, and the thermal conductivity, respectively. The dashed line indicates no-use in this simulation. The details of the functional dependencies on the temperature and of the parameter values are mentioned in Refs. 21 and 22.

Parameters	Poly-Si	Fine-Si	a-Si	Liquid-Si	Glass
$\alpha(\text{cm}^{-1})$	$1.9 \times 10^4 - 4.7 \times 10^5$	...	...	$1.13 \times 10^6$	...
$n$	4.168–4.237	...	...	2.35	1.46
$\kappa$	0.08–2.0	...	...	4.8	0
$L(\text{J/g})$	1800	1800	1320	...	...
$T_m(^{\circ}\text{C})$	1410	1410	1150	...	...
$\rho(\text{g/cm}^3)$	2.33	2.33	2.33	2.33	2.33
$c_p(\text{J/g K})$	0.7–1	0.7–1	0.7–1	1	0.38
$K(\text{J/s cm K})$	0.75–0.12	0.05	0.01	0.25–0.42	0.0025

zero order and first order and is proportional to the amplitude of the surface corrugation  $h$ . The details are mentioned in Ref. 20. This equation indicates that a spatially sinusoidal laser energy density profile with spacing  $\Lambda$  exists on the surface in addition to  $P_0$ . Also,  $\phi_p = \pm 180^\circ$  correspond to energy being absorbed more in the "hills" than in the "valleys" of the corrugation while  $\phi_p = 0$  corresponds to just the opposite situation. Hereafter, we use this normal modulated Poynting component,  $P_n$ , as the spatially sinusoidal laser energy density profile.

$$\rho \frac{h_{i,j}^{(t+1)} - h_{i,j}^{(t)}}{\Delta t} = \frac{1}{(\Delta x)^2} \left( \frac{K_{i+1,j} + K_{i,j}}{2} (T_{i+1,j}^{(t)} - T_{i,j}^{(t)}) + \frac{K_{i,j} + K_{i-1,j}}{2} (T_{i-1,j}^{(t)} - T_{i,j}^{(t)}) \right) + \frac{1}{(\Delta z)^2} \left( \frac{K_{i,j+1} + K_{i,j}}{2} (T_{i,j+1}^{(t)} - T_{i,j}^{(t)}) + \frac{K_{i,j} + K_{i,j-1}}{2} (T_{i,j-1}^{(t)} - T_{i,j}^{(t)}) \right) + S_{i,j}^{(t)}, \quad (4)$$

according to the model developed by Wood and Geist.<sup>21</sup> Here,  $\Delta x$  and  $\Delta z$  are very small dimensions along the  $x$  and  $z$  axes, respectively,  $h_{i,j}^{(t)}$  is the enthalpy of  $(i,j)$  cell with the area of  $\Delta x \times \Delta z$  at the time  $t$ ,  $\rho$  is the density of the material,  $K_{i,j}$  is the temperature-dependent thermal conductivity,  $T_{i,j}^{(t)}$  is the temperature, and  $S_{i,j}^{(t)}$  is the heat source term that includes the absorption of the incident laser radiation. Basically, at every time step  $\Delta t$ , the model calculates the temperature profile of all cells, taking the profile of the pulse laser energy density into account. Then, the phase change and the release of latent heat in each cell are simulated by considering its temperature and comparing it with its neighbors using the state array matrix (see Ref. 21). This matrix contains the information of the phase diagram of the amorphous-Si (a-Si)/poly-Si/liquid-Si system and one time  $t_n$ . The time  $t_n$  is used to simulate spontaneous nucleation event. It is defined as the incubation time required for the appearance of nucleation sites in the supercooled liquid-Si and corresponds to the inverse of the bulk nucleation rate. The supercooled liquid-Si is liquid phase whose temperature is lower than the crystallization temperature of 1410 °C. A nucleation condition of this model is as follows: when the temperature of supercooled liquid-Si becomes lower than the so-called nucleation temperature  $T_n$ , the nucleation timer starts to count. A nucleation occurs when the timer passes the nucleation time  $t_n$ . This nucleation condition cannot simulate a nucleation event completely because an actual nucleation might occur randomly regardless of  $T_n$ . However, it is considered that the simulation results based on this condition are not so far from an actual nucleation. The grain boundary forms only at the position where the liquid-solid interface cannot move any longer due to its being surrounded by the solid phase. The  $\Delta x$  and  $\Delta z$  are 10 and 5 nm, respectively, and the time step  $\Delta t$  is  $1 \times 10^{-13}$  s which is smaller than the stability criterion for this finite elements system. On this calculation, we focus a poly-Si film state crystallized with some pulses. This is because we confirmed experimentally that the initial a-Si film

## B. Temperature profile and crystallization process

We assume that a temperature profile generated by our method varies in both the  $x$  and  $z$  directions in Eq. (2) although the actual beam energy density profile of a Nd:YAG laser is Gaussian-like. This assumption is adequate if we focus on the local area less than a few tens of micrometer size because the experimental beam size is about 10 mm. The two-dimensional finite difference heat transport equation is given by

was completely melted and changed to polycrystalline after the first pulse irradiation for our experimental condition and the periodic grain boundaries began to form after the second pulse irradiation. Also, the complete melting of the initial a-Si is simulated not only because of its higher absorption coefficient (about  $10^5$ – $10^6$  cm<sup>-1</sup>)<sup>22</sup> than that of poly-Si (about  $10^4$ – $10^5$  cm<sup>-1</sup>) but also its lower melting temperature (1150 °C)<sup>21</sup> than that of poly-Si (1410 °C). The typical simulation conditions are as follows: the nucleation time  $t_n$  is 8 ns estimated from the experimental data, the nucleation temperature  $T_n$  is 1250 °C,<sup>21</sup> the substrate is a fused quartz which does not change its phase at any time, the laser energy density is 150 mJ/cm<sup>2</sup>, and the substrate temperature is 220 °C of our experimental condition. The spatial energy density profile of the pulse laser beam is  $P_n$  of Eq. (3) and its time-dependent intensity profile is a Gaussian function with a full width at half maximum of 6.5 ns and a base line of 13 ns. The material parameters used in this simulation are summarized in Table I.

## III. EXPERIMENT

An a-Si film was deposited on a Pyrex glass at 350 °C in an ultrahigh-vacuum chamber. The deposition rate and pressure were 1 nm/s and  $1 \times 10^{-7}$  Pa, respectively. After deposition, the a-Si film was irradiated by a linearly polarized Nd:YAG pulse laser (wavelength: 532 nm, repetition frequency: 10 Hz, pulse width: 6–7 ns) at 220 °C in the same chamber. The shape of the laser beam was Gaussian-like with a 10-mm diameter. The other laser irradiation conditions were as follows: the a-Si thickness was 60 nm, the laser energy density  $F$  was 150 mJ/cm<sup>2</sup> which was not an average but a local value on the Gaussian profile, the irradiation pulse number  $N$  was 10–100, and the beam incident angle  $\theta_i$  was 0° and 25°. After melting crystallization, some samples were Secco etched in order to delineate the grain boundary. The surface morphology was characterized by scanning electron microscope (SEM) and atomic force microscope (AFM).

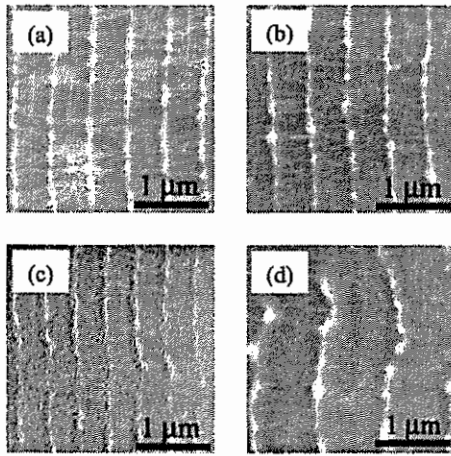


FIG. 2. SEM images of the Secco-etched Si films crystallized at (a)  $\theta_i=0$  and  $N=10$ , (b)  $\theta_i=0$  and  $N=100$ , (c)  $\theta_i=25^\circ$  and  $N=10$ , and (d)  $\theta_i=25^\circ$  and  $N=100$ .

Since the periodic grain boundary that is typically the last to freeze during lateral grain growth have accumulated Si, i.e., corrugations due to the squeezing of the expanding solid in the remaining liquid-Si,<sup>23</sup> the surface roughness around the grain boundary is higher than that of the other area. Therefore, we can find the location of the grain boundary by measuring the surface morphology of non-Secco-etched sample with AFM.

#### IV. RESULTS

Figures 2(a) and 2(b) show the SEM images of Secco-etched Si films crystallized with  $\theta_i=0$  at  $N=10$  and 100, respectively, and Figs. 2(c) and 2(d) show those with  $\theta_i=25^\circ$  at  $N=10$  and 100, respectively. It can be clearly noticed from Fig. 2 that although the periodic widths of the grain boundary,  $\Lambda$ , of Figs. 2(a) and 2(b) at  $\theta_i=0$  are the same even for different  $N$ , those of Figs. 2(c) and 2(d) at  $\theta_i=25^\circ$  are different from each other, where  $\Lambda$  of Figs. 2(c) and 2(d) are about  $370 \text{ nm} \approx 532/(1+\sin 25^\circ)$  and about  $900 \text{ nm} \approx 532/(1-\sin 25^\circ)$ , respectively. This result suggests that the periodic width  $\Lambda$  depends on the pulse number  $N$  at  $\theta_i \neq 0$ . Also, it can be clearly seen that while the grain boundaries for the normal incidence run straight in parallel to one another irrespective of the pulse number, those at  $\theta_i=25^\circ$  and  $N=100$  of Fig. 2(d) are curvedly aligned. Their periodic width is fluctuated from 800 to 1100 nm, centered around 920 nm, calculated from  $\lambda/(1-\sin \theta_i)$  at  $\theta_i=25^\circ$ . However, even at  $\theta_i=25^\circ$ , as shown in Fig. 2(c), the grain boundaries are aligned not curvedly but straight when the  $N$  is reduced to 10.

In order to estimate more strictly the spatial period of the surface roughness of the laser-crystallized Si film, as shown in Figs. 2(c) and 2(d), we performed Fourier analysis of the surface morphology measured by AFM. Figure 3(a) shows the measured surface morphologies of the as-deposited a-Si film and Si films crystallized with  $\theta_i=25^\circ$  at  $N=10$  and 100, and Fig. 3(b) shows the relationship between the Fourier coefficient and the spatial period  $\Lambda$ , where the samples are not Secco etched. We can see from Fig. 3(a) that the surfaces

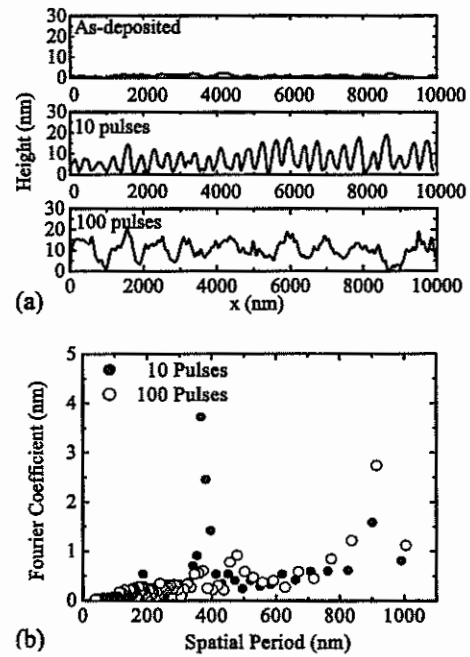


FIG. 3. (a) Measured surface morphologies of the as-deposited Si film and the Si films crystallized with  $\theta_i=25^\circ$  at  $N=10$  and 100. (b) Relationship between the Fourier coefficient and the spatial period of the measured surface roughness, where the closed square is for as deposited and the closed and open circles are for  $N=10$  and 100, respectively.

of the Si films crystallized with  $\theta_i=25^\circ$  at  $N=10$  and 100 have a definite periodic surface structure although the as-deposited a-Si film has random roughness with the small height. It is also found from Fig. 3(b) that the two large peaks appear around 370 and 900 nm in the crystallized films, corresponding to Rayleigh's diffraction conditions of Eq. (1). At  $N=10$ , the Fourier coefficient for  $\Lambda=370 \text{ nm}$  is much larger than that for 900 nm but the situation at  $N=100$  becomes the opposite. In other words, the  $\lambda/(1+\sin \theta_i)$  component of Eq. (1) is predominant for small  $N$  but it is suppressed for large  $N$ .

#### V. DISCUSSION

In this section, we will discuss the reasons not only for the fluctuation in the periodic grain boundaries formed at the irradiation conditions of  $\theta_i=25^\circ$  and  $N=100$  as shown in Fig. 2(d) but also for the dependence of the Fourier coefficient on the pulse number  $N$ . At first, we carried out the theoretical calculation of the spatially sinusoidal laser energy density profile,  $P_n$ . Figures 4(a) and 4(b) show the calculated results of the dependencies of the ac amplitude ratio  $P_1$  and the phase  $\phi_p$  of  $P_n$  on the spatial period  $\Lambda$ , respectively, where a laser beam with  $\lambda=532 \text{ nm}$  is irradiated at  $\theta_i=25^\circ$  on a weakly corrugated poly- or liquid-Si surface with  $h=1.5 \text{ nm}$ . From Fig. 4(a), we can see two obvious resonances in the  $P_1$  of both the Si states around the spatial periods calculated from Eq. (1) and they are indicated by the two vertical dotted lines as well as in Fig. 4(b) of  $\phi_p$ .

##### A. Controllability of grain-boundary location

It can be seen from Fig. 4(b) that any  $\phi_p$  is not equal to  $\pm 180^\circ$  at  $\theta_i=25^\circ$ , which means that the energy density pro-

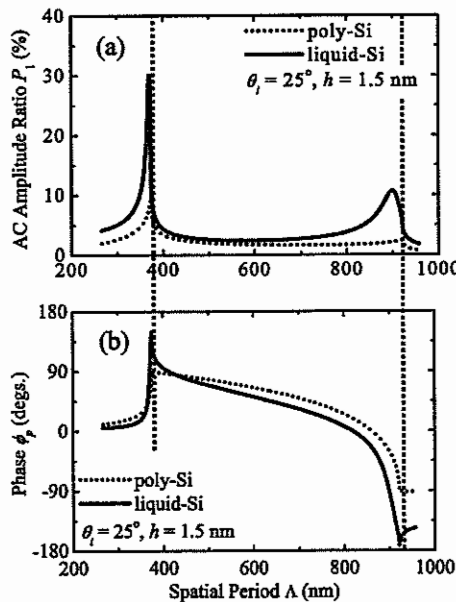


FIG. 4. Dependencies of (a) the ac amplitude ratio  $P_1$  and (b) the phase  $\phi_p$  of  $P_n$  at the sinusoidal corrugated surface of a poly- and liquid-Si on the spatial period  $\Lambda$ , where the laser beam is  $\lambda=532$  nm,  $h=1.5$  nm, and  $\theta_i=25^\circ$ . The refractive indexes  $\epsilon$  for poly- and liquid-Si are  $17.24+i0.66$  and  $-17.52+i22.56$ , respectively.

file or the temperature profile does not coincide with the original surface corrugation in phase. It is well known that a grain boundary is formed around the position of maximum temperature for a melting-crystallized Si film because the solidification or crystal growth propagates from low- to high-temperature region in the film. This suggests that the location of the grain boundary may be changed at each pulse irradiation with  $\theta_i=25^\circ$ . In order to simulate the process of the grain-boundary formation in the case of  $\phi_p \neq \pm 180^\circ$ , we performed the two-dimensional computer calculation using the  $P_n$  for poly-Si before surface melting of the Si film and for liquid-Si after melting with  $h=5$  nm. Figure 5 depicts the cross sections of the initial state of a poly-Si film before laser beam irradiation (upper) and its crystallized state after irradiation (lower), where the  $\Lambda=910$  nm  $\approx 532/(1-\sin 25^\circ)$  and each Si film is drawn for only one spatial period. The initial state is hypothetical without grain boundary in spite of poly-Si film. A solid curve on the top is  $P_n$  due to the laser

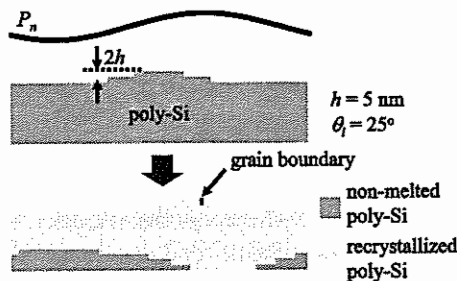


FIG. 5. Simulated states of the cross-sectional crystallized Si films with  $\Lambda=910 \approx 532/(1-\sin 25^\circ)$  nm and  $h=5$  nm. The upper part shows the initial poly-Si film before irradiation of the laser beam whose energy density profile is represented as a solid curve above it. This initial film is a virtual state and nonmelted crystallized poly-Si. The lower part is the recrystallized film after irradiation. The recrystallized and nonmelted poly-Si states are distinguished by the grey scales on the right-hand side of the lower part.

irradiation. Since this simulation gives us grain-boundary positions but does not take into account the mass transport during the melting crystallization, we construct the surface corrugation artificially by using the following procedure. The surface of the crystallized Si film has one corrugation with the height of  $2h$  on one grain boundary determined by the simulation. The corrugation shape is Gaussian with the full width at half maximum of 130 nm, which is a typical value of our crystallized Si film, and  $h$  is set to be 5 nm. Because the initial state has no grain boundary, a surface corrugation is formed virtually at the center. The simulation of temperature profile and crystallization process takes into account the geometrical surface corrugation. Although it can be seen from Fig. 2 that the actual grain boundaries run through the film from the bottom to the surface, the simulated boundary of Fig. 5 is presented not as a vertical line but as a point. This is because the definition of the grain-boundary position in the simulation is the final liquid cell  $\Delta x \Delta y$  surrounded by solid phase, as mentioned in Sec. II B, which is different from the real phenomena, as mentioned in Ref. 23. However, this definition can be considered to be enough for qualitative discussion in our case. It is found from the lower simulation result of the crystallized film that one grain boundary is formed not at the previous position of the upper case but at the position on the maximum laser energy density. This means that the amplitude of the spatially sinusoidal energy density profile is large enough to control the direction of the lateral crystal growth of the Si film. Also, this result suggests that the grain-boundary location should move forward or backward in the normal direction of the boundary line on each successive laser shot, as shown in Fig. 2(d). That is, the fluctuation of the grain-boundary line results when the difference in phase  $\phi_p$  is not  $\pm 180^\circ$  between  $P_n$  and the surface corrugation of Eq. (2). On the other hand, the grain boundaries of the Si film crystallized at  $\theta_i=25^\circ$  and  $N=10$  are hardly fluctuated, as shown in Fig. 2(c) in spite of  $\phi_p \neq \pm 180^\circ$ . This is probably due to a small pulse number  $N$ . Generally, the deviation parts from the straight line of the grain boundary are increased with increasing  $N$ , which means that the fluctuation of the grain-boundary alignment is enhanced with  $N$ . However, in the case of Fig. 2(c), since  $N$  is a small number, 10, the fluctuation is little. Further, the  $P_1$  for  $\Lambda=370$  nm is much larger compared with that for the other  $\Lambda$ , as shown in Fig. 4(a), that the controllability in the direction of crystal growth from the liquid phase is strong. Therefore, the grain boundaries at  $\theta_i=25^\circ$  and  $N=10$  are not so fluctuated. In the case of  $\theta_i=0$ , because the  $\phi_p$  is calculated to be  $\pm 180^\circ$ , the grain boundary is always formed in the same position at each pulse and its line is straight for any  $N$ , as shown in Figs. 2(a) and 2(b). Also, in the simulation after crystallization of Fig. 5, nonmelted poly-Si regions exist at the bottom of the film because the laser energy density is not high enough to melt the whole poly-Si film completely.

## B. Periodic grain-boundary width

Next, we discuss the dependence of the Fourier coefficient on the pulse number  $N$ , as shown in Fig. 3. Since the calculated  $P_1$  for  $\Lambda \approx 370$  nm is much larger than that for



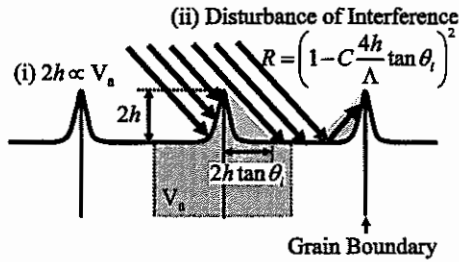


FIG. 6. Schematic drawing of the model to explain the dependence of the dominant periodic width of the grain boundary on the pulse number  $N$ . The height  $2h$  of the surface corrugation on a grain boundary is proportional to the average molten Si volume,  $V_a$ , between the two neighbor grains bounded by the grain boundaries. The disturbance factor  $R$  of the interference between the incident and the diffracted beams is  $[1 - C(4h/\Lambda)\tan\theta_i]^2$ , where  $C$  is a correction constant.

$\Lambda \approx 900$  nm. as shown in Fig. 4(a), it can be easily understood that the  $\lambda/(1+\sin\theta_i)$  component is predominant for small  $N$ . However, this reason is not valid for the experimental result of large  $N$ . In order to explain the result for large  $N$  physically, we propose a model, as illustrated schematically in Figs. 6 and 7. In this model, we consider three factors that influence the determination of  $\Lambda$ . The first is that the corrugation height  $2h$  on the grain boundary is proportional to the average volume,  $V_a$ , of the two molten Si regions bounded by the two neighbor grain boundaries, as shown in Figs. 6 and 7 schematically. Generally, it is considered that the corrugation is formed by lateral liquid mass transport during the melting-crystallization process<sup>23</sup> and its amount is supplied from a molten Si region bounded by the two nucleation sites, as shown in the upper part of Fig. 7. Although it is supposed in general that the nucleation site is located on the minimum temperature of the temperature profile, it is not always true. For example, when some part of the Si film is completely melted from the bottom to the surface, the random nucleation sometimes occurs due to supercooling, irrespective of the temperature profile. Also, nucleation easily occurs at the in-

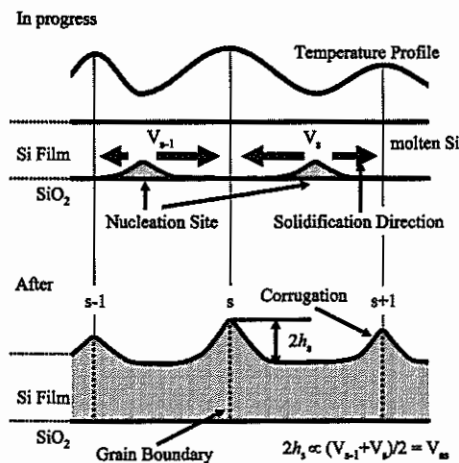


FIG. 7. Schematic drawings of the model to explain the formation of the surface corrugation on the grain boundary due to the mass transport of liquid-Si during melting-crystallization process. In the upper part, the nucleation sites and solidification directions are indicated in the molten Si film under some temperature profile. In the lower part, the corrugation height  $2h_s$  on the grain boundary,  $s$ , is proportional to the average molten Si volume between  $V_s$  and  $V_{s-1}$ .

terface between the melted and nonmelted regions compared with the completely melted region. In fact, when the Si film is not completely melted, as shown in the lower part of Fig. 5, the nucleation sites are not only at the lower temperature but also at other locations depending on the surface structure, energy density profile, supercooling in the small complete-melting region, and so on. So, as the nucleation site, we used a statically average one of the middle of the grain. In practice, as shown in Fig. 7, the corrugation height  $2h_s$  on the grain boundary,  $s$ , is proportional to  $(V_s + V_{s-1})/2 = V_a$ , where  $V_s$  and  $V_{s-1}$  are the molten Si volumes in the regions between the boundary  $s$  and  $s+1$ , and  $s-1$  and  $s$ , respectively. The molten Si are produced from the Si film melted by laser irradiation and we can estimate the molten volume by using crystallization process analysis in Sec. II.

The second factor is that  $P_1$  is not monotonously proportional to the amplitude  $h$  of the corrugated surface, which is different from the theoretical analysis of Sec. II. In fact, it has been reported that the validity in the theoretical analysis of the modulation of the Poynting vector or spatial energy density profile on the corrugated surface is limited to the condition of a small  $h/\Lambda$ .<sup>24,25</sup> The surface corrugation makes a shaded area on the surface and prevents the reflected beam from propagating, as shown in Fig. 6. The  $(4h \tan\theta_i)/\Lambda$  is the geometrical-optical ratio of the twice-shaded length to  $\Lambda$  and has a physical meaning of a disturbance ratio to the full interference. Thus, we define a correction factor  $R$  as

$$R = \left(1 - C \frac{4h}{\Lambda} \tan\theta_i\right)^2, \quad (5)$$

where  $C$  is a correction constant to indicate the degree of the disturbance effect on interference. For example,  $C=0$ ,  $C=1$ , and  $C>1$  mean no disturbance to interference, disturbance only due to surface roughness, and disturbance due to not only surface roughness but also other effects, respectively. Also, the square in Eq. (5) is to make  $R$  a power factor. In the actual calculation,  $P_1$  in Eq. (3) is replaced with  $RP_1$ , which reduces the interference effect by a factor of  $R$  related with  $h$ .

On the other hand, it has been reported that the surface morphology changes after melting due to viscosity of liquid-Si, i.e., the surface roughness of the Si film gets reduced during liquid phase.<sup>23</sup> Because  $P_1$  is proportional to the height of the surface corrugation, the third factor is to consider the surface morphology change during crystallization process. The damping coefficient  $\gamma$  for surface roughness reduction can be calculated from

$$\gamma = \frac{8\pi^2 v}{\Lambda^2 \rho} \quad (6)$$

according to the Ref. 23, where  $v$  is the viscosity. Using the measured viscosity (0.7 mPa/s)<sup>26</sup> and density (2.53 g/cm<sup>3</sup>)<sup>23</sup> of the liquid-Si, the relaxation times,  $\tau = 1/\gamma$ , are estimated to be 6.3 and 37 ns for the spatial periods  $\Lambda = 370$  and 900 nm, respectively. Because the estimated  $\tau$  for  $\Lambda = 370$  nm is much shorter than that for 900 nm, it is considered that the contribution from the liquid corrugation to the periodic temperature profile for 370 nm is smaller than that for 900 nm. Also, it is known that this damping coefficient  $\gamma$  depends on the

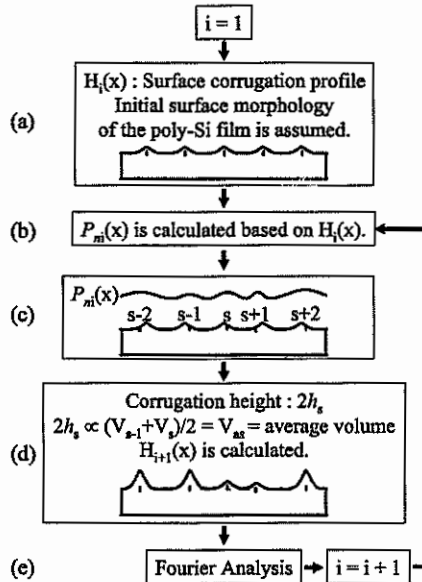


FIG. 8. Flow chart of the simulation sequence. The simulation is performed one pulse by one pulse. At first, (a) the initial corrugation height profile  $H_1(x)$  for  $i=1$  is hypothesized. Then, (b) we calculate the laser energy density profile  $P_n(x)$  based on  $H_1(x)$  and (c) simulate the melting-crystallized process and the grain-boundary locations. Next, (d) using the average molten Si volume,  $H_{i+1}(x)$  is calculated and (e) Fourier analyzed. After that, we reset  $i=i+1$  and continue the simulation.

melting depth of the Si film and our simulation shows that it takes about 2 ns to reach a maximum melting depth after the surface melting starts. So, in this simulation, after a delay time,  $t_m$ , from the whole Si surface melting,  $P_n$  of liquid-Si is calculated in consideration of the exponential reduction of the liquid surface roughness with time constant  $\tau$  at each simulation time step for simplicity. The simulation was performed one pulse by one pulse and the calculation sequence is shown in Fig. 8. The energy density profile generated on the sample surface was assumed to be made up from the superposition of the two  $P_n$  for  $\Lambda=370 \text{ nm} \approx \lambda(1 + \sin \theta_i)$  and  $\Lambda=900 \text{ nm} \approx \lambda(1 - \sin \theta_i)$  components. This is because  $P_n$  for the other spatial periodicity components are negligibly small compared with the above two components, as shown in Fig. 4(a). Also, since the least common multiple of 370 and 900 nm is too large to calculate effectively, we set the calculation width to be 1800 nm which is the least common multiple of 360 and 900 nm. It can be considered that the approximation of 370–360 nm is not an essential issue geometrically. However, because  $P_1$  and  $\phi_p$  strongly depend on  $\Lambda$ , as shown in Fig. 4, those not for  $\Lambda=360 \text{ nm}$  but for 370 nm were used. At  $i=1$ , the periodic grain-boundary positions are set with  $\Lambda=360$  and 900 nm virtually, and the surface corrugations are constructed on each grain boundary artificially, assuming the corrugation volume is 10% of the average molten Si volume  $V_a$  [Fig. 8(a)]. This initial virtual state is poly-Si film without laser irradiation. As the initial surface morphology conditions at  $i=1$ , i.e., the Fourier coefficients for  $\Lambda=360$  and 900 nm are the same, 1 nm. According to the surface corrugation profile  $H_1(x)$ , the laser energy density profile  $P_{n1}(x)$  is calculated [Fig. 8(b)], and the boundary positions and their widths are determined by using the theoretical analysis of Sec. II [Fig. 8(c)]. Then, we calculate the

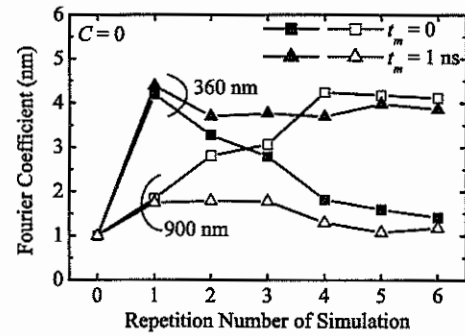


FIG. 9. Simulation results of the repetition number dependencies of the Fourier coefficients for  $\Lambda=360$  (closed) and 900 nm (open) with  $C=0$ , where the squares and triangles are for  $t_m=0$  and 1 ns, respectively.

corrugation height profile  $H_2(x)$  using the assumption of  $2h_s \propto (V_{s-1} + V_s)/2 = V_{as}$  [Fig. 8(d)]. Using the  $H_2(x)$ , we perform the Fourier analysis to this surface corrugation and we obtain Fourier coefficients or  $h$  for  $\Lambda=360$  and 900 nm [Fig. 8(e)]. For the next pulse, we set  $i=i+1$  and repeat the same simulation procedure from Fig. 8(b), using the surface morphology and the Fourier coefficients obtained from the last simulation.

Figure 9 shows the dependencies of the Fourier coefficients of the crystallized Si film surface on the repetition number of simulation,  $N_R$ , for  $\Lambda=360$  and 900 nm. In order to examine the effect of  $t_m$  on the Fourier coefficient,  $t_m$  was set to 0 or 1 ns with  $C=0$  although  $C=0$  means ignoring interference disturbance due to surface roughness. It can be seen from Fig. 9 that, for  $t_m=0$ , the Fourier coefficients for  $\Lambda=900 \text{ nm}$  (open squares) gradually increase with  $N_R$  and the Fourier coefficients for  $\Lambda=360 \text{ nm}$  (closed squares) gradually decrease with  $N_R$  after  $N_R=1$ . On the other hand, for  $t_m=1 \text{ ns}$ , the Fourier coefficients for  $\Lambda=900 \text{ nm}$  (open triangles) and 360 nm (closed triangles) remain small and large, respectively, regardless of  $N_R$ . At  $N_R=1$ , the Fourier coefficients for  $\Lambda=360 \text{ nm}$  for both  $t_m$  increase abruptly, which means that the grain boundaries with  $\Lambda=360 \text{ nm}$  are formed in the main. This is because the amplitude of periodic laser energy density profile for  $\Lambda=360 \text{ nm}$  is much larger than that for 900 nm, as shown in Fig. 4(a). It is further because we hypothesized the initial surface morphology that the heights for  $\Lambda=360$  and 900 nm are the same, 1 nm, and that the ratio of the number of the grain boundary with the 360-nm width to that with the 900-nm width is  $900:360=2.5:1$ . This initial condition is further different from the experimental results such as Fig. 3 which shows that the height for  $\Lambda=370 \text{ nm}$  is much larger than that for  $\Lambda=900 \text{ nm}$  for small  $N$ . Therefore, due to the first simulation of  $N_R=1$ , the simulated surface morphology drastically changes from the initial one and approaches the experimental one. It can be said that the simulation resets the surface morphology of the poly-Si film from the initial artificial state to the real or plausible state for small  $N$ . Also, the height for  $\Lambda=360 \text{ nm}$  at  $N_R=1$  is almost the largest among other  $N_R$  and a nearly saturated value because the periodic grain boundaries with the 360-nm width are mainly formed over the calculation width of 1800 nm due to much larger  $P_1$  for  $\Lambda=360 \text{ nm}$  than that for 900 nm. However, increasing  $N_R$ ,



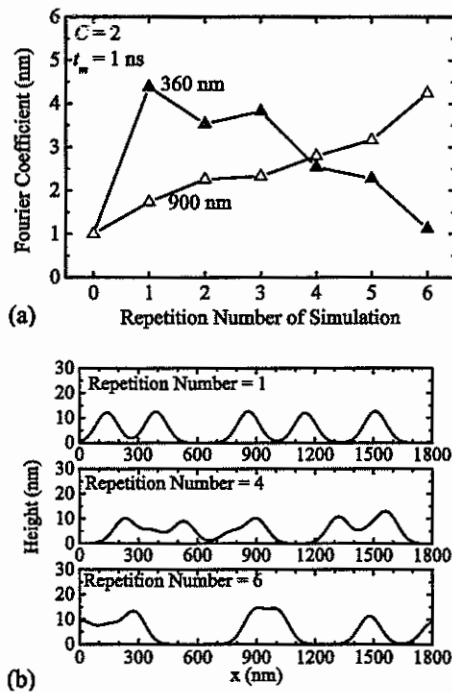


FIG. 10. Simulation results of (a) the repetition number dependencies of the Fourier coefficients for  $\Lambda=360$  and 900 nm, and (b) the surface morphologies for the calculation repetition numbers of 1, 4, and 6, where  $C=2$  and  $t_m=1$  ns.

the height for  $\Lambda=360$  nm is suppressed but that for 900 nm is increased gradually, as shown in Fig. 9 ( $t_m=0$ ). One of the reasons is that the damping effect on liquid surface roughness for  $\Lambda=360$  nm is much more effective than that for 900 nm. The higher damping leads to lower amplitude of the periodic temperature profile, which hardly forms grain boundary with its period. The other reason is that the  $P_1$  for  $\Lambda=360$  nm has already reached a nearly saturated value at  $N_R=1$  and is hardly increased from the value while the  $P_1$  for 900 nm is possible to increase due to the positive feedback loop, as mentioned in Sec. II. Also, the damping effect on  $P_1$  is more enhanced by decreasing  $t_m$  because the irradiation time during high surface roughness of liquid state is shortened. Therefore, the Fourier coefficients for  $\Lambda=360$  nm and  $t_m=0$  decrease with  $N_R$  although that for  $t_m=1$  ns is almost constant.

Since the periodic energy density profile is formed by interference between the incident beam and the diffracted beam on the surface, the surface roughness is an actual obstacle to the interference. So,  $C=0$  might be impossible physically. Also, it is hardly supposed that the reduction of the surface roughness due to liquid viscosity occurs as soon as the surface is molten because the film body except for the surface is still in the solid state. Considering the simulation result of about 2 ns to reach a maximum melting depth after the surface melting starts, we set  $t_m$  to be 1 ns as a reasonable average time. Then, we tried to simulate, using  $t_m=1$  ns for  $C=1$  and 2. The simulation result for  $C=1$  was almost similar to Fig. 9 ( $t_m=1$  ns) which does not show the tendency of the experimental results. Figures 10(a) and 10(b) show the dependencies of the Fourier coefficients for  $\Lambda=360$  and 900 nm on the repetition number and the calculated surface mor-

phologies for  $N_R=1, 4$ , and 6, respectively, where  $C=2$  and  $t_m=1$  ns. We can see from Fig. 10(a) that the Fourier coefficient for  $\Lambda=360$  nm rises up rapidly at  $N_R=1$  like Fig. 9 ( $t_m=1$  ns) but decreases gradually with  $N_R \geq 2$  while that for 900 nm increases gradually with  $N_R$ . At  $N_R=6$ , the coefficient for  $\Lambda=900$  nm becomes predominant, which is roughly similar to the experimental results of Fig. 3(b). Also, from Fig. 10(b), it can be seen that the number and the space of the corrugation decreases and increases, respectively, with increasing  $N_R$ , which shows the same tendency of the experimental result of Fig. 3(a). In this simulation, the concept of thermal diffusion length influences tacitly. The diffusion length is calculated to be nearly equal to the short  $\Lambda=370$  nm and it reduces the amplitude ratio of the periodic temperature profile between  $\Lambda=370$  and 900 nm, compared with the  $P_1$  ratio between them. Further, as can be seen from Fig. 4(a), the peak width of  $P_1$  around 370 nm is much narrower than that around 900 nm. This suggests that the interference resonance around 370 nm is broken more easily than that around 900 nm due to the fluctuation of  $\Lambda$ , which leads to one possible reason for the reasonable simulation result with  $C=2$ . That is, the fluctuation of  $\Lambda$  in the actual crystallization is one of the other disturbance effects on interference. Since, in this simulation, the model for the formation of the surface corrugation after laser irradiation is rough and not strict, this result cannot perfectly follow the experimental results like Fig. 3. Indeed, the simulation result of Fig. 10(a) shows that the faster transition in periodic grain-boundary width from  $\Lambda=370$  to 900 nm occurs with smaller  $N_R$ , in other words, smaller irradiation pulse number  $N$ , compared with the experimental result. This is mainly because the mass-transport phenomenon is not taken into account strictly in the simulation. However, the simulation results reveal the similar tendency to the experimental data, i.e., the periodic grain-boundary width  $\Lambda$  for small  $N$  is near  $\lambda/(1+\sin \theta_i)$ , and  $\Lambda$  for large  $N$  is near  $\lambda/(1-\sin \theta_i)$ . Therefore, it can be said that our model expresses physical phenomenon essentially.

## VI. CONCLUSION

We investigated the periodic grain-boundary formation in the poly-Si film crystallized by a linearly polarized Nd:YAG pulse laser beam with the oblique incidence, comparing with the normal incidence. The experimental results were discussed with the theoretical calculation of the two-dimensional numerical simulation. We found that the fluctuation in the grain-boundary line was caused mainly by non-phase matching between the corrugated surface and the periodic temperature profile. The nonphase matching arises not in the normal incident case but in the oblique incident case. When the phase difference between them is out of  $\pm 180^\circ$ , the grain-boundary is subjected to moving forward and backward in the normal direction of the grain boundary line on successive shots. Therefore, the grain-boundary location is fluctuated more with larger  $N$  for the oblique incidence. Also, it was found that the dominant spatial period of the grain boundary in the crystallized Si film depended on the irradiation pulse number  $N$ . Actually, it was 370

$\approx 532/(1 + \sin 25^\circ)$  nm at  $N=10$  and  $900 \approx 532(1 - \sin 25^\circ)$  nm at  $N=100$ . This dependence can be explained by the next factors. (i) The amplitude ratio of the periodic laser energy density profile,  $P_1$ , for  $\Lambda=370$  nm is much larger than that for 900 nm if the surface corrugation heights,  $2h$ , for both the cases are equal, (ii) the height of the corrugated surface on a grain boundary is proportional to the average volume of the two molten Si regions surrounded by the neighbor grain boundaries, (iii) the actual  $P_1$  on the surface is reduced with increasing  $h$ , (iv) the  $P_1$  in the liquid phase is decreased exponentially with time due to the surface roughness reduction caused by the liquid viscosity, and (v) the thermal diffusion length during the pulse width is nearly equal to the short  $\Lambda=370$  nm.

## ACKNOWLEDGMENTS

This work was partly supported by the Sasakawa Scientific Research Grant from the Japan Science Society. Also, the authors would like to thank Mr. Y. Nakata and T. Ootani for the preparation and observation of some samples in the Department of Materials Science of Japan Advanced Institute of Science and Technology.

- <sup>1</sup>T. Sameshima, S. Usui, and M. Sekiya, *IEEE Electron Device Lett.* **7**, 276 (1986).
- <sup>2</sup>K. Sera, F. Okumura, H. Uchida, S. Itoh, S. Kaneko, and K. Hotta, *IEEE Electron Device Lett.* **36**, 2868 (1989).
- <sup>3</sup>H. J. Kim and J. S. Im, *Appl. Phys. Lett.* **68**, 1513 (1996).
- <sup>4</sup>M. Ozawa, C.-H. Oh, and M. Matsumura, *Jpn. J. Appl. Phys., Part 1* **38**, 5700 (1999).
- <sup>5</sup>A. Hara and N. Sasaki, *Jpn. J. Appl. Phys., Part 2* **39**, L1 (2000).
- <sup>6</sup>D.-H. Choi, K. Shimizu, O. Sugiura, and M. Matsumura, *Jpn. J. Appl.*

- Phys., Part 1, Part 1* **31**, 4545 (1992).
- <sup>7</sup>K. Shimizu, O. Sugiura, and M. Matsumura, *IEEE Electron Device Lett.* **40**, 112 (1993).
- <sup>8</sup>R. Ishihara and P. Ch. van der Wilt, *Jpn. J. Appl. Phys., Part 2* **37**, L15 (1998).
- <sup>9</sup>L. Mariucci, R. Carluccio, A. Pecora, V. Foglietti, G. Fortunato, and D. D. Sala, *Jpn. J. Appl. Phys., Part 2* **38**, L907 (1999).
- <sup>10</sup>B. Rezek, C. E. Nebel, and M. Stutzmann, *Jpn. J. Appl. Phys., Part 2* **38**, L1083 (1999).
- <sup>11</sup>C.-H. Oh, M. Ozawa, and M. Matsumura, *Jpn. J. Appl. Phys., Part 2* **37**, L492 (1998).
- <sup>12</sup>S. Horita, Y. Nakata, and A. Shimoyama, *Appl. Phys. Lett.* **78**, 2250 (2001).
- <sup>13</sup>M. Oron and G. Sørensen, *Appl. Phys. Lett.* **35**, 782 (1979).
- <sup>14</sup>J. F. Young, J. E. Sipe, J. S. Preston, and H. M. van Driel, *Appl. Phys. Lett.* **41**, 261 (1982).
- <sup>15</sup>J. F. Young, J. S. Preston, H. M. van Driel, and J. E. Sipe, *Phys. Rev. B* **27**, 1155 (1983).
- <sup>16</sup>A. E. Siegman and P. M. Fauchet, *IEEE J. Quantum Electron.* **22**, 1384 (1986).
- <sup>17</sup>Y. Kawakami, E. Ozawa, and S. Sasaki, *Appl. Phys. Lett.* **74**, 3954 (1999).
- <sup>18</sup>P. E. Dyer and R. J. Farley, *Appl. Phys. Lett.* **57**, 765 (1990).
- <sup>19</sup>Y. Nakata, H. Kaki, and S. Horita, *Jpn. J. Appl. Phys., Part 1* **43**, 2630 (2004).
- <sup>20</sup>Z. Guosheng, P. M. Fauchet, and A. E. Siegman, *Phys. Rev. B* **26**, 5366 (1982).
- <sup>21</sup>R. F. Wood and G. A. Geist, *Phys. Rev. B* **34**, 2606 (1986).
- <sup>22</sup>G. Aichmayr, D. Toet, M. Mulato, P. V. Santos, A. Spangenberg, S. Christiansen, M. Albrecht, and H. P. Strunk, *J. Appl. Phys.* **85**, 4010 (1999).
- <sup>23</sup>D. K. Fork, G. B. Anderson, J. B. Boyce, R. I. Johnson, and P. Mei, *Appl. Phys. Lett.* **68**, 2138 (1996).
- <sup>24</sup>R. Petit and M. Cadilhac, *C. R. Seances Acad. Sci., Ser. B* **262**, 468 (1966).
- <sup>25</sup>A. Wirgin, *Opt. Acta* **27**, 1671 (1980).
- <sup>26</sup>H. Sasaki, E. Tokizaki, X. M. Huang, K. Terashima, and S. Kimura, *Jpn. J. Appl. Phys., Part 1* **34**, 3432 (1995).